Analysis of Activity Dips in Quartz Crystal Microbalances under Temperature Bias Fields Using the Lee Plate Model

Mengjie Li[a], Nian Li[b, *], Peng Li[a], Hirotsugu Inoue[c], Iren Kuznetsova[d], Dianzi Liu[e], Zhenghua Qian[a, *]

[a] State Key Laboratory of Mechanics and Control for Aerospace Structures, College of Aerospace Engineering, Nanjing University of Aeronautics and Astronautics, Nanjing, 210016, China

[b] School of Mechanical Engineering, Suzhou University of Technology, Changshu, 215500, China

[c] Department of Mechanical Engineering, Institute of Science Tokyo, Tokyo, 152-8552, Japan

[d] Kotel'nikov Institute of Radio Engineering and Electronics of RAS, Moscow, 125009, Russia

[e] School of Engineering, University of East Anglia, Norwich, NR4 7TJ, U. K.

[*]Corresponding author, E-mail address: qianzh@nuaa.edu.cn, nianli@szut.edu.cn.

Tel.: +86-25-84895952, Fax: +86-25-84891422.

Abstract High-frequency quartz crystal microbalances (QCMs) operating in the thickness-shear mode exhibit pronounced frequency-temperature behavior, particularly in ultrathin plates. Since frequency-temperature stability is strongly influenced by structural dimensions, temperature variations modify the electromechanical coupling and mode interactions of quartz, thereby affecting the electrical response of QCMs. In this study, the Lee plate model incorporating temperature bias fields is developed to analyze the vibrational and electrical responses of QCMs with and without electrodes. The novelty of this work lies in establishing a mathematically consistent plate formulation that captures temperature dependent mode coupling and electrical response without empirical correction factors. Its correctness is validated through dispersion analysis of infinite quartz plates and formulated as a system of partial differential equations (PDEs) for free and forced vibration analysis. Results reveal that strong mode coupling induced by structural dimensions and intensified by temperature variations leads to significant loss of mass sensitivity over a limited temperature range. Moreover, the resonant frequency associated with the admittance peak and the electrical response amplitude become highly sensitive to the absorbed mass under temperature bias fields. These findings provide a rigorous mathematical explanation for temperature-induced activity dips and electrical anomalies in high-frequency QCMs.

Keywords: Quartz crystal microbalance, Lee plate theory, mode coupling, mass sensitivity, electrical response.

1. Introduction

Quartz crystal microbalance (QCM), as a typical thickness-shear mode quartz crystal resonator, are widely employed for high-precision mass sensing due to their excellent sensitivity and frequency stability. In high-frequency devices, frequency stability and electrical reliability are particularly sensitive to external temperature variations, and the frequency-temperature behavior becomes increasingly complex as the operating frequency increases. To investigate mode coupling and energy-trapping characteristics, a two-dimensional cross-sectional model is commonly adopted, formulated using elastic theory or plate theory. For high-frequency applications, plate theory is generally preferred because of its higher computational efficiency and easier implementation of mode coupling analysis. In these resonators, geometric parameters such as the plate thickness, length-to-thickness ratio, electrode coverage, and absorbed mass play a critical role in determining resonance characteristics, and the influence of these parameters become increasingly significant as the resonant frequency increases, especially in ultrathin plates. Meanwhile, temperature variations also modify the material stiffness, piezoelectric coupling, and damping, which in turn affect vibrational displacements and electrical admittance responses. Therefore, accurate modeling of the interaction between structural parameters and temperature-dependent material properties is crucial for understanding the vibrational and electrical behavior of high-frequency QCMs.

Beyond conventional mass detection [1, 2], QCMs are also employed in

biomedical sensing [3, 4] and liquid property analysis [5, 6], highlighting their broad applicability. Under ideal conditions, the mass sensitivity of QCMs follows the Sauerbrey relation [7], which establishes a linear relationship between mass change on the electrode surface and the corresponding frequency shift [8, 9]. However, this proportional relationship is strongly influenced by temperature variations, which may compromise frequency stability and reduce measurement accuracy. With advances in precision quartz cutting and ultrathin fabrication, high-frequency QCMs exceeding 100 MHz have been realized [10], exhibiting enhanced sensitivity and high quality factors, while their temperature-dependent behavior is commonly analyzed using elastic theory incorporating thermal effects [11]. Early investigations of thermal effects mainly focused on free vibration analysis of quartz structures [12-14] or different crystal cuts [15, 16]. Although Mindlin plate theory combined with incremental thermal effects has been used [17, 18], temperature-dependent corrections to the cutoff frequency are required and therefore, this theory is not suitable for high-order plate formulations. Meanwhile, advanced thermoelastic and heat transfer models, including multi-phase lag and microstructural formulations [19-21] as well as nonlocal and memory-dependent heat transfer theories [22, 23], further underscore the importance of rigorous thermal-mechanical coupling for accurate vibration analysis under thermal effects. In contrast, the Lee plate theory systematically approximates the three-dimensional elastic wave equations by expanding displacements into trigonometric series and linear functions of the plate thickness [24, 25]. By introducing a linear term to account for in-plane displacements associated with normal rotations, a unified framework for

analyzing both frequency-temperature characteristics and electrical behavior was established by Peter C Y. Lee [26]. The Lee plate theory accurately captures high-frequency thickness modes, boundary effects, and electromechanical coupling under temperature bias fields without requiring correction coefficients [27], while maintaining consistency and computational efficiency [28, 29]. The first-order Lee plate equations provide resonant frequency solutions that closely match exact solutions [30], and incorporating fully covered electrodes significantly improves the prediction accuracy of resonant frequencies [31]. Later, Wu et al. [32] extended the Lee plate theory to SC cut quartz plates with partial electrodes. Based on the incremental thermal field theory developed by Lee and Yong [33], Wang further derived thermally coupled Lee plate equations by expanding incremental displacements along the thickness direction using trigonometric series, and analyzed the frequency-temperature relationship of quartz crystal plates [34]. By integrating incremental thermal effects into the Lee plate framework, this approach enables comprehensive evaluation of temperature influences on the vibrational and electrical responses of quartz resonators, thereby providing a reliable theoretical basis for high-frequency QCM applications.

Despite these advances, comprehensive investigations that simultaneously considers thermal bias fields, strong mode coupling, and adsorbed mass effects in high-frequency QCMs remains limited. In particular, the mechanisms through which mode coupling-induced by temperature variations leads to sensitivity loss, activity dips, and electrical response anomalies have not been systematically clarified within a unified framework. In this study, first-order Lee plate formulation incorporating incremental

thermal effects is employed to analyze finite QCMs with and without electrodes. The main contributions of this study are as follows. First, a unified model is established to consistently couple the thermal bias, electromechanical interaction, and mass loading. Second, the relationship between the plate aspect ratio and strong mode coupling induced by temperature variations is quantitatively revealed, together with the resulting sensitivity loss. Third, the influence of the adsorbed mass on electrical stability and admittance characteristics under temperature variations is clarified. The proposed approach provides a coherent explanation of temperature-dependent activity dips and anomalous electrical behavior within a mode coupling framework, and offers practical guidance for selecting structural parameters, , avoiding the occurrence of unstable operating regions in high-frequency QCM devices.

2. Lee plate equation considering temperature bias field

Assume that there is a temperature biasing field, the incremental thermal field of a three-dimensional linear piezoelectric body can be consistently formulated through the equations of motion, electrostatics, geometry, and constitutive relations [35], expressed as follows:

$$\begin{aligned} &\beta_{ik}T_{kj,j} = \rho\ddot{u}_i, \\ &D_{i,i} = 0, \end{aligned} \tag{1a}$$

$$\begin{aligned} T_{ij} &= c^{\theta}_{ijkl}S_{kl} - e^{\theta}_{kij}E_k, \\ D_i &= e^{\theta}_{ijk}S_{jk} + \varepsilon^{\theta}_{ik}E_k, \end{aligned} \tag{1b}$$

$$S_{ij} = \frac{1}{2}\left(\beta_{kj}u_{k,i} + \beta_{ki}u_{k,j}\right), \qquad E_i = -\phi_{,i}. \tag{1c}$$

where T_{ij}, D_i, S_{ij} and E_i represents stress, electric displacement, strain, and electric field, respectively. ρ denotes the material density. c^{θ}_{ijkl}, e^{θ}_{ijk}, $\varepsilon^{\theta}_{ij}$ and β_{ij} mean the temperature-dependent elastic constant, piezoelectric constant, dielectric constant, and thermal expansion coefficient, respectively. u_i means the displacement, and a superscript dot indicates the partial derivative with respect to time, i.e., $\partial/\partial t$. ϕ represents the electric potential, and a subscript comma indicates the derivative with respect to the coordinate component x_i. Using tensor notation, i, j, k and l take the value of 1, 2, or 3, respectively.

The piezoelectric material parameters [35] related to temperature are formulated as follows:

$$\begin{aligned} c^{\theta}_{ijkl} &= c_{ijkl} + c^{(1)}_{ijkl}\Delta T + c^{(2)}_{ijkl}\Delta T^2 + c^{(3)}_{ijkl}\Delta T^3, \\ e^{\theta}_{ijk} &= e_{ijk} + e^{(1)}_{ijk}\Delta T + e^{(2)}_{ijk}\Delta T^2 + c^{(3)}_{ijk}\Delta T^3, \\ \varepsilon^{\theta}_{ik} &= \varepsilon_{ik} + \varepsilon^{(1)}_{ik}\Delta T + \varepsilon^{(2)}_{ik}\Delta T^2 + \varepsilon^{(3)}_{ik}\Delta T^3, \\ \beta_{ik} &= \delta_{ik} + \alpha^{(1)}_{ik}\Delta T + \alpha^{(2)}_{ik}\Delta T^2 + \alpha^{(3)}_{ik}\Delta T^3. \end{aligned} \tag{2}$$

where c_{ijkl}, e_{ijk}, and ε_{ik} are the elastic constant, piezoelectric constant and dielectric constant at room temperature (25°C), respectively. $c^{(n)}_{ijkl}$, $e^{(n)}_{ijk}$ and $\varepsilon^{(n)}_{ij}$ mean the nth-order thermoelastic constants, nth-order temperature derivative of the piezoelectric constants, and nth-order temperature coefficients of the dielectric permittivity constants, respectively. δ_{ik} represents the Kronecker delta, and $\alpha^{(n)}_{ik}$ is the nth-order thermal expansion coefficients of quartz. The temperature change $\Delta T = T - T_0$ is defined, where T and T_0 are the initial and reference temperatures, respectively, and T_0 is equal to 25°C.

For a piezoelectric solid with the volume V and bounded by the surface S, mechanical boundary conditions require the displacement and stress continuities,

whereas electrical boundary conditions demand the continuity of electric potential under either short-circuit or specified states.

The continuity of boundary conditions are defined by Eq. (3)

$$\begin{aligned} u_i &= \hat{u}_i, \\ \phi &= \hat{\phi}, \\ t_i &= n_j \beta_{ik} T_{kj}, \\ \sigma &= n_i D_i. \end{aligned} \tag{3}$$

According to the divergence equation in V and boundary conditions on S derived by Tiersten [36] using the variational principle, two equations are formulated as follows:

$$\begin{aligned} &\int_{t_0}^{t} dt \int_V [(\beta_{ik} T_{kj,j} - \rho \ddot{u}_i)\delta u_j + D_{i,i}\delta\phi] dV = 0, \\ &\int_{t_0}^{t} dt \int_S [(t_j - n_j \beta_{ik} T_{kj})\delta u_j + (\sigma - n_i D_i)\delta\phi] dS = 0. \end{aligned} \tag{4}$$

where t_j and σ represent the surface traction and surface charge density, respectively. n_i means the unit outward normal to S.

As illustrated in Fig. 1, the three-dimensional plate is determined in a rectangular coordinate system x_i. The displacement and electric potential of the plate are expressed in a function of trigonometric series expansions along the plate thickness. For a quartz crystal plate with the partial electrode, the potential in the region covered by the electrode (denoted as ϕ^e) is expanded in terms of sinusoidal functions to satisfy the zero-potential boundary condition [26], whereas the potential in the non-electrode region (denoted as ϕ^u) is represented by the sum of cosine expansions [37]. The detailed expressions are mathematically defined as follows:

$$
\begin{aligned}
u_i(x_1,x_2,x_3,t) &= \sum_{n=0}^{\infty}(u_i^{(n)}(x_1,x_3,t) - bc_n u_{2,i}^{(0)})\cos\frac{n\pi}{2}(1-\psi),\\
\phi^e(x_1,x_2,x_3,t) &= A(t) + B(t)\psi + \sum_{n=0}^{\infty}\phi^{(n)}(x_1,x_3,t)\sin\frac{n\pi}{2}(1-\psi),\\
\phi^u(x_1,x_2,x_3,t) &= \sum_{n=0}^{\infty}\phi^{(n)}(x_1,x_3,t)\cos\frac{n\pi}{2}(1-\psi),\\
c_n &= \int_{-1}^{1}\psi\cos\frac{n\pi}{2}(1-\psi)d\psi = \begin{cases} 8/(n^2\pi^2), & n = \text{odd} \\ 0, & n = \text{even} \end{cases}.
\end{aligned}
\tag{5}
$$

where $\psi = x_2/b$, and b is half the plate thickness. $u_i^{(n)}$ and $\phi^{(n)}$ are the n-order displacement and potential components, respectively, which are in functions of x_1, x_3 and t.

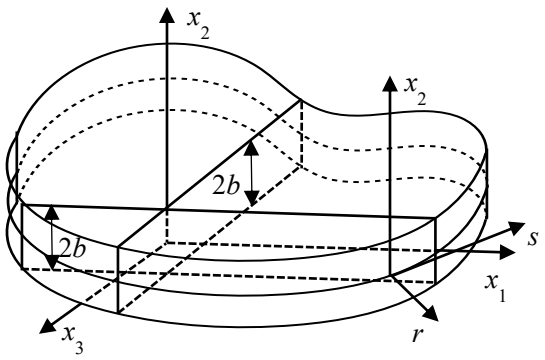

Fig. 1. 3D structure of the uniform plate.

Substituting Eq. (5) into Eq. (1c), one can obtain:

$$
\begin{aligned}
S_{ij} &= \sum_{n=0}^{\infty}\left[S_{ij}^{(n)}\cos\frac{n\pi}{2}(1-\psi) + \bar{S}_{ij}^{(n)}\sin\frac{n\pi}{2}(1-\psi)\right],\\
E_i &= \sum_{n=0}^{\infty}\left[\bar{E}_i^{(n)}\cos\frac{n\pi}{2}(1-\psi) + E_i^{(n)}\sin\frac{n\pi}{2}(1-\psi)\right].
\end{aligned}
\tag{6}
$$

Therefore, the strain and electric field components associated with the n-order incremental thermal field in the Lee plate equations, considering both electrode-free and electrode cases, are transformed into Eq. (6):

$$
\begin{aligned}
&\bar{S}_{ij}^{(n)} = \frac{n\pi}{4b}\left(\beta_{kj}\delta_{2i}(u_k^{(n)} - bc_n u_{2,k}^{(0)}) + \beta_{ki}\delta_{2j}(u_k^{(n)} - bc_n u_{2,k}^{(0)})\right),\\
&S_{ij}^{(n)} = \frac{1}{2}\left[\beta_{kj}u_{k,i}^{(n)} + \beta_{ki}u_{k,j}^{(n)} - bc_n(\beta_{kj}u_{2,ki}^{(0)} + \beta_{ki}u_{2,kj}^{(0)})\right],\\
&\bar{E}_i^{(n)} = -\frac{B(t)}{b}\delta_{2i}\delta_{n0} + \delta_{2i}\frac{n\pi}{2b}\phi^{(n)},\ E_i^{(n)} = -\phi_{,i}^{(n)}, \qquad \text{(with electrode)}\\
&E_i^{(n)} = -\frac{B(t)}{b}\delta_{2i}\delta_{n0} - \phi_{,i}^{(n)},\ \bar{E}_i^{(n)} = -\delta_{2i}\frac{n\pi}{2b}\phi^{(n)}. \quad \text{(without electrode)}
\end{aligned}
\tag{7}
$$

Assume that $dV = dAdx_2$ and $dA = dx_1dx_3$ are defined [26], with the integration along the plate thickness x_2, the following two-dimensional divergence theory is reformulated by substituting Eq. (5) into the variational equation (4):

$$
\int_A f_{b,b}dA = \int_C n_b f_b dS. \tag{8}
$$

It is noted that the trigonometric relationships are defined as follows:

$$
\begin{aligned}
&\int_{-1}^{1}\sin\frac{m\pi}{2}(1-\psi)\sin\frac{n\pi}{2}(1-\psi)d\psi = \delta_{mn} - \delta_{m0}\delta_{n0},\\
&\int_{-1}^{1}\cos\frac{m\pi}{2}(1-\psi)\cos\frac{n\pi}{2}(1-\psi)d\psi = \delta_{mn} + \delta_{m0}\delta_{n0}.
\end{aligned}
\tag{9}
$$

The variational forms of the equations of motion and electrostatic equations in the incremental thermal field are derived:

$$
\begin{aligned}
&\int_{t_0}^{t_1}dt\int_A\sum_{n=0}^{\infty}\left[\begin{array}{l}[\beta_{ik}T_{kj,j}^{(n)} + \frac{1}{b}\beta_{ik}F_k^{(n)} - \frac{n\pi}{2b}\beta_{ik}\bar{T}_{2k}^{(n)} - (1+\delta_{n0})\rho(\ddot{u}_i^{(n)} - bc_n\ddot{u}_{2,i}^{(0)})]\delta u_i^{(n)}\\ -[\beta_{ik}T_{kj,j}^{(n)} + \frac{1}{b}\beta_{ik}F_k^{(n)} - \frac{n\pi}{2b}\beta_{ik}\bar{T}_{2k}^{(n)} - (1+\delta_{n0})\rho(\ddot{u}_i^{(n)} - bc_n\ddot{u}_{2,i}^{(0)})]bc_n\delta u_{2,i}^{(0)}\end{array}\right]dA\\
&+\int_{t_0}^{t_1}dt\int_A\sum_{n=0}^{\infty}\left\{\bar{D}_{a,a}^{(n)} + \frac{n\pi}{2b}D_2^{(n)}\right\}\delta\phi^{(n)}dA = 0, \qquad \text{(with electrode)}\\
&\int_{t_0}^{t_1}dt\int_A\sum_{n=0}^{\infty}\left[\begin{array}{l}[\beta_{ik}T_{kj,j}^{(n)} + \frac{1}{b}\beta_{ik}F_k^{(n)} - \frac{n\pi}{2b}\beta_{ik}\bar{T}_{2k}^{(n)} - (1+\delta_{n0})\rho(\ddot{u}_i^{(n)} - bc_n\ddot{u}_{2,i}^{(0)})]\delta u_i^{(n)}\\ -[\beta_{ik}T_{kj,j}^{(n)} + \frac{1}{b}\beta_{ik}F_k^{(n)} - \frac{n\pi}{2b}\beta_{ik}\bar{T}_{2k}^{(n)} - (1+\delta_{n0})\rho(\ddot{u}_i^{(n)} - bc_n\ddot{u}_{2,i}^{(0)})]bc_n\delta u_{2,i}^{(0)}\end{array}\right]dA\\
&+\int_{t_0}^{t_1}dt\int_A\sum_{n=0}^{\infty}\left\{D_{a,a}^{(n)} - \frac{n\pi}{2b}\bar{D}_2^{(n)} + \frac{1}{b}D^{(n)}\right\}\delta\phi^{(n)}dA = 0. \qquad \text{(without electrode)}
\end{aligned}
\tag{10}
$$

where a = 1 or 3. The stress, face-traction and electric displacement components are defined by Eq. (11):

$$
\begin{aligned}
&T_{ij}^{(n)} = \int_{-1}^{1} T_{ij}\cos\frac{n\pi}{2}(1-\psi)d\psi,\ \ \bar{T}_{ij}^{(n)} = \int_{-1}^{1} T_{ij}\sin\frac{n\pi}{2}(1-\psi)d\psi,\\
&F_j^{(n)} = T_{2j}(b) - (-1)^n T_{2j}(-b),\\
&D_i^{(n)} = \int_{-1}^{1} D_i\cos\frac{n\pi}{2}(1-\psi)d\psi,\ \ \bar{D}_i^{(n)} = \int_{-1}^{1} D_i\sin\frac{n\pi}{2}(1-\psi)d\psi,\\
&D^{(n)} = D_2(b) - (-1)^n D_2(-b).
\end{aligned}
\tag{11}
$$

For independent variations of $\delta(u_j^{(n)} - bc_n u_{2,j}^{(0)})$ and $\delta\phi_j^{(n)}$ in Eq. (10), the n-order equations of motion and electrostatic equation considering the incremental thermal field can be obtained:

$$
\begin{aligned}
&\beta_{ik}T_{kj,j}^{(n)} + \frac{1}{b}\beta_{ik}F_k^{(n)} - \frac{n\pi}{2b}\beta_{ik}\bar{T}_{2k}^{(n)} - (1+\delta_{n0})\rho(\ddot{u}_i - bc_n\ddot{u}_{2,i}^{(0)}) = 0,\\
&\begin{cases}
\bar{D}_{a,a}^{(n)} + \dfrac{n\pi}{2b}D_2^{(n)} = 0, & \text{(with electrode)}\\
D_{a,a}^{(n)} - \dfrac{n\pi}{2b}\bar{D}_2^{(n)} + \dfrac{1}{b}D^{(n)} = 0. & \text{(without electrode)}
\end{cases}
\end{aligned}
\tag{12}
$$

Substituting Eqs. (6) and (7) into Eq. (1b), the stress component and electric displacement component considering the incremental thermal field in the Lee plate theory are obtained:

$$
\begin{cases}
T_{ij}^{(n)} = \sum_{m=0}^{\infty}(\delta_{mn}+\delta_{m0}\delta_{n0})(c_{ijkl}^{\theta}S_{kl}^{(m)} - e_{kij}^{\theta}\bar{E}_k^{(m)}) + \sum_{m=0}^{\infty}B_{mn}(c_{ijkl}^{\theta}\bar{S}_{kl}^{(m)} - e_{kij}^{\theta}E_k^{(m)}),\\
\bar{T}_{ij}^{(n)} = \sum_{m=0}^{\infty}(\delta_{mn}-\delta_{m0}\delta_{n0})(c_{ijkl}^{\theta}\bar{S}_{kl}^{(m)} - e_{kij}^{\theta}E_k^{(m)}) + \sum_{m=0}^{\infty}B_{nm}(c_{ijkl}^{\theta}S_{kl}^{(m)} - e_{kij}^{\theta}\bar{E}_k^{(m)}),\\
D_i^{(n)} = \sum_{m=0}^{\infty}(\delta_{mn}+\delta_{m0}\delta_{n0})(e_{ijk}^{\theta}S_{jk}^{(m)} + \varepsilon_{ik}^{\theta}\bar{E}_k^{(m)}) + \sum_{m=0}^{\infty}B_{mn}(e_{ijk}^{\theta}\bar{S}_{jk}^{(m)} + \varepsilon_{ik}^{\theta}E_k^{(m)}),\\
\bar{D}_i^{(n)} = \sum_{m=0}^{\infty}(\delta_{mn}-\delta_{m0}\delta_{n0})(e_{ijk}^{\theta}\bar{S}_{jk}^{(m)} + \varepsilon_{ik}^{\theta}E_k^{(m)}) + \sum_{m=0}^{\infty}B_{nm}(e_{ijk}^{\theta}S_{jk}^{(m)} + \varepsilon_{ik}^{\theta}\bar{E}_k^{(m)}),
\end{cases}
\quad \text{(with electrode)}
$$

$$
\begin{cases}
T_{ij}^{(n)} = \sum_{m=0}^{\infty}(\delta_{mn}+\delta_{m0}\delta_{n0})(c_{ijkl}^{\theta}S_{kl}^{(m)} - e_{kij}^{\theta}E_k^{(m)}) + \sum_{m=0}^{\infty}B_{mn}(c_{ijkl}^{\theta}\bar{S}_{kl}^{(m)} - e_{kij}^{\theta}\bar{E}_k^{(m)}),\\
\bar{T}_{ij}^{(n)} = \sum_{m=0}^{\infty}(\delta_{mn}-\delta_{m0}\delta_{n0})(c_{ijkl}^{\theta}\bar{S}_{kl}^{(m)} - e_{kij}^{\theta}\bar{E}_k^{(m)}) + \sum_{m=0}^{\infty}B_{nm}(c_{ijkl}^{\theta}S_{kl}^{(m)} - e_{kij}^{\theta}E_k^{(m)}),\\
D_i^{(n)} = \sum_{m=0}^{\infty}(\delta_{mn}+\delta_{m0}\delta_{n0})(e_{ijk}^{\theta}S_{jk}^{(m)} + \varepsilon_{ik}^{\theta}\bar{E}_k^{(m)}) + \sum_{m=0}^{\infty}B_{mn}(e_{ijk}^{\theta}\bar{S}_{jk}^{(m)} + \varepsilon_{ik}^{\theta}E_k^{(m)}),\\
\bar{D}_i^{(n)} = \sum_{m=0}^{\infty}(\delta_{mn}-\delta_{m0}\delta_{n0})(e_{ijk}^{\theta}\bar{S}_{jk}^{(m)} + \varepsilon_{ik}^{\theta}E_k^{(m)}) + \sum_{m=0}^{\infty}B_{nm}(e_{ijk}^{\theta}S_{jk}^{(m)} + \varepsilon_{ik}^{\theta}\bar{E}_k^{(m)}),
\end{cases}
\quad \text{(without electrode)}
\tag{13}
$$

where, the constant B_{mn} is as follows:

$$B_{mn}=\int_{-1}^{1}\sin\frac{m\pi}{2}(1-\psi)\cos\frac{n\pi}{2}(1-\psi)d\psi=\begin{cases}4m/(m^2-n^2)\pi, & m+n=\text{odd}\\ 0, & m+n=\text{even}\end{cases} \tag{14}$$

Substituting Eq. (13) into Eq. (4), boundary conditions considering the thermal effect can be obtained on the basis of the above assumptions and similar derivation process. Also, the conditions of 2D (surface) and 1D (edge) interfaces are defined by Eqs. (15) and (16), respectively:

$$\begin{aligned} &t_i=n_j\beta_{ik}T_{kj} \ \text{ or } \ u_i=\hat{u}_i,\\ &\phi=\hat{\phi}. \end{aligned} \tag{15}$$

$$\begin{aligned} &t_r^{(n)}=n_r\beta_{rk}T_{kr}^{(n)} \ \text{ or } u_r^{(n)}-bc_nu_{2,r}^{(0)}=\hat{u}_r^{(n)}-bc_n\hat{u}_{2,r}^{(0)},\\ &t_s^{(n)}=n_r\beta_{sk}T_{kr}^{(n)} \ \text{ or } \ u_s^{(n)}=\hat{u}_s^{(n)},\\ &\delta_{n0}bc_nt_{s,s}^{(n)}+t_2^{(n)}=\delta_{n0}bc_n\beta_{sk}T_{kr,s}^{(n)}+\beta_{2k}T_{kr}^{(n)} \ \text{ or } \ u_2^{(n)}=\hat{u}_2^{(n)},\\ &\bar{\sigma}^{(n)}=n_i\bar{D}_i^{(n)} \ \text{ or } \ \phi^{(n)}=\hat{\phi}^{(n)}. \end{aligned} \tag{16}$$

where *r* and *s* denote the directions normal and tangential to the edge, respectively (see Fig. 1).

3. First-order Lee plate equation

Generally, a QCM consists of a quartz crystal plate with electrodes on both sides. The reason for the selection of the AT-cut quartz crystal operating with thickness-shear mode lies in its stable frequency-temperature behavior. Fig. 2 shows the schematic diagram of QCM with the adsorbed mass layer. The thickness and length of the quartz crystal plate are $h_q = 2b = 0.033$mm and $l_q = 1.2$mm, respectively. The thicknesses of the upper and lower electrodes are $h_{e1} = 100$nm and $h_{e2} = 200$nm, with the electrode length l_e of 0.7mm. The density of quartz ρ_q is 2649kg/m^3. The electrode material

property is silver, with the density of ρ_e is 10490kg/m^3.

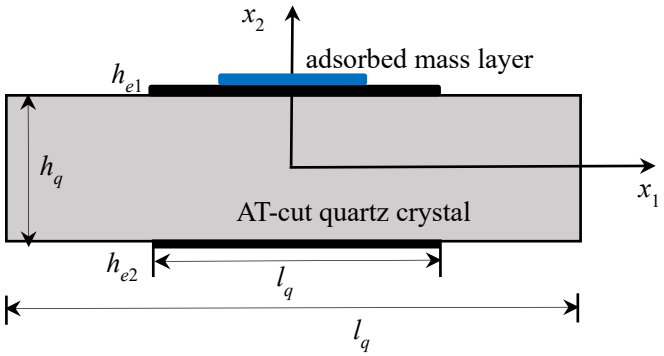

Fig. 2. Schematic diagram of the QCM structure for detecting adsorbed mass layer.

Retaining the first two terms in the Lee plate equations considering the incremental thermal field described in Section 2, the first-order governing equations are obtained. Using the displacement expansion defined in Eq. (5), the corresponding displacement and electric potential are given by:

$$\begin{aligned} &u_1^{(n)},\ u_3^{(n)} = 0 \quad (n>1), \quad u_2^{(n+1)} = 0, \quad \phi^{(n+1)} = 0 \ (n>1) \\ &T_{22}^{(1)} = 0, \quad u_2^{(2)} = 0, \quad \text{but } u_2^{(2)} \neq 0. \end{aligned} \tag{17}$$

Assume that the straight-crested wave propagates along the x_1-axis, a coupling of modes arise in the AT-cut quartz crystal plate, specifically the flexural (F), face-shear (FS), and first-order thickness-shear (TSh1) modes. Their associated displacement components [38] are denoted as $u_2^{(0)}$, $u_3^{(0)}$ and $u_1^{(1)}$. Hence, the displacements are linearly approximated by:

$$\begin{aligned} u_1(x_1,x_2,x_3,t) &= (u_1^{(1)}(x_1,x_3,t) - bc_1 u_{2,1}^{(0)})\cos\frac{\pi}{2}(1-\psi), \\ u_2(x_1,x_2,x_3,t) &= u_2^{(0)}(x_1,x_3,t), \\ u_3(x_1,x_2,x_3,t) &= u_3^{(0)}(x_1,x_3,t). \end{aligned} \tag{18}$$

Combining with Eq. (18), the geometrical equation of the first-order Lee plate theory considering the incremental thermal field is defined:

$$
\begin{aligned}
&\bar{s}_{12}^{(1)} = \frac{\pi}{4b}\beta_{11}(u_1^{(1)} - bc_1 u_{2,1}^{(0)}),\\
&s_{12}^{(0)} = \frac{1}{2}(\beta_{22}u_{2,1}^{(0)} + \beta_{23}u_{3,1}^{(0)}),\quad s_{13}^{(0)} = \frac{1}{2}(\beta_{23}u_{2,1}^{(0)} + \beta_{33}u_{3,1}^{(0)}),\\
&s_{11}^{(1)} = \beta_{11}(u_{1,1}^{(1)} - bc_1 u_{2,11}^{(0)}).
\end{aligned}
\tag{19}
$$

The boundary conditions are:

$$
\begin{aligned}
&t_1^{(n)} = n_1\beta_{11}T_{11}^{(1)} \ \text{ or } \ u_1^{(1)} - bc_1u_{2,1}^{(0)} = \hat{u}_1^{(1)} - bc_1\hat{u}_{2,1}^{(0)},\\
&t_3^{(0)} = n_1\beta_{23}T_{12}^{(0)} + n_1\beta_{33}T_{13}^{(0)} \ \text{ or } \ u_3^{(0)} = \hat{u}_3^{(0)},\\
&t_2^{(0)} = \beta_{22}T_{12}^{(0)} + \beta_{23}T_{13}^{(0)} \quad \text{or} \quad u_2^{(0)} = \hat{u}_2^{(0)},\\
&\bar{\sigma}^{(2)} = n_1\bar{D}_1^{(2)} \quad \text{or} \quad \phi^{(2)} = \hat{\phi}^{(2)}.
\end{aligned}
\tag{20}
$$

Thus, the potential of first-order Lee plate in the region covered by electrode is formulated as follows:

$$
\phi^e(x_1,x_2,x_3,t) = A(t) + B(t)\psi + \phi^{(1)}(x_1,x_3,t)\sin\frac{\pi}{2}(1-\psi) + \phi^{(2)}(x_1,x_3,t)\sin\pi(1-\psi). \tag{21}
$$

In the non-electrode region, the potential is given by:

$$
\phi^u(x_1,x_2,x_3,t) = \phi^{(1)}(x_1,x_3,t)\cos\frac{\pi}{2}(1-\psi) + \phi^{(2)}(x_1,x_3,t)\cos\pi(1-\psi). \tag{22}
$$

Accordingly, the relations between the electric field and the potential are defined as follows:

$$
\begin{aligned}
&\bar{E}_2^{(0)} = -\frac{B(t)}{b},\ \bar{E}_2^{(1)} = -\frac{\pi}{2b}\phi^{(1)},\ \bar{E}_2^{(2)} = \frac{\pi}{b}\phi^{(2)},\\
&E_1^{(1)} = -\phi_{,1}^{(1)},\ E_1^{(2)} = -\phi_{,1}^{(2)}.
\end{aligned}
\tag{23}
$$

For the first-order Lee plate theory considering the incremental thermal field in the region covered by the electrode, only the electrode mass effect is considered while the elastic effects are neglected. The motion of equations and electrostatics equations are formulated as:

$$
\begin{aligned}
&\beta_{22}T_{12,1}^{(0)}+\beta_{23}T_{13,1}^{(0)}-2\rho(1+R+R_g)\ddot{u}_2^{(0)}=0,\\
&\beta_{32}T_{12,1}^{(0)}+\beta_{33}T_{13,1}^{(0)}-2\rho(1+R+R_g)\ddot{u}_3^{(0)}=0,\\
&\beta_{11}T_{11,1}^{(1)}-\frac{\pi}{2b}\beta_{11}\bar{T}_{21}^{(1)}+\rho bc_1\ddot{u}_{2,1}^{(0)}-\rho(1+2R+2R_g)\ddot{u}_1^{(1)}=0,\\
&\bar{D}_{1,1}^{(2)}+\frac{\pi}{b}D_2^{(2)}=0.
\end{aligned}
\tag{24}
$$

where, the adsorbed mass layer is represented by the mass ratio R_g. R denotes the mass ratio of the electrodes to the quartz crystal, defined by $R = \rho_e\ (h_{e1}+ h_{e2})/\ (\rho_q\ h_q)$.

The motion equations and electrostatics equations in the non-electrode region are derived as follows:

$$
\begin{aligned}
&\beta_{22}T_{12,1}^{(0)}+\beta_{23}T_{13,1}^{(0)}-2\rho\ddot{u}_2^{(0)}=0,\\
&\beta_{32}T_{12,1}^{(0)}+\beta_{33}T_{13,1}^{(0)}-2\rho\ddot{u}_3^{(0)}=0,\\
&\beta_{11}T_{11,1}^{(1)}-\frac{\pi}{2b}\beta_{11}\bar{T}_{21}^{(1)}+\rho(bc_1\ddot{u}_{2,1}^{(0)}-\ddot{u}_1^{(1)})=0,\\
&D_{1,1}^{(1)}-\frac{\pi}{2b}\bar{D}_2^{(1)}=0.
\end{aligned}
\tag{25}
$$

Also, the constitutive equations of the first-order Lee plate theory considering the incremental thermal field in the region covered by the electrode are described as follows:

$$
\begin{aligned}
&T_{12}^{(0)}=4c_{66}^{\theta}s_{12}^{(0)}+4c_{56}^{\theta}s_{13}^{(0)}+\frac{8}{\pi}c_{66}^{\theta}\bar{s}_{12}^{(1)}-2e_{26}^{\theta}\bar{E}_2^{(0)},\\
&T_{13}^{(0)}=4c_{56}^{\theta}s_{12}^{(0)}+4c_{55}^{\theta}s_{13}^{(0)}+\frac{8}{\pi}c_{56}^{\theta}\bar{s}_{12}^{(1)}-2e_{25}^{\theta}\bar{E}_2^{(0)},\\
&T_{11}^{(1)}=c_{11}^{\theta}s_{11}^{(1)}-\frac{8}{3\pi}e_{11}^{\theta}E_1^{(2)},\\
&\bar{T}_{21}^{(1)}=2c_{66}^{\theta}\bar{s}_{12}^{(1)}+\frac{8}{\pi}c_{66}^{\theta}s_{12}^{(0)}+\frac{8}{\pi}c_{56}^{\theta}s_{13}^{(0)}-\frac{4}{\pi}e_{26}^{\theta}\bar{E}_2^{(0)}+\frac{4}{3\pi}e_{26}^{\theta}\bar{E}_2^{(2)},\\
&\bar{D}_1^{(2)}=\frac{8}{3\pi}e_{11}^{\theta}s_{11}^{(1)}+\varepsilon_{11}^{\theta}E_1^{(2)},\\
&D_2^{(2)}=-\frac{8}{3\pi}e_{26}^{\theta}\bar{s}_{12}^{(1)}+\varepsilon_{22}^{\theta}\bar{E}_2^{(2)},\\
&D_2^{(0)}=2e_{26}^{\theta}s_{12}^{(0)}+2e_{25}^{\theta}s_{13}^{(0)}+\varepsilon_{22}^{\theta}\bar{E}_2^{(0)}+\frac{8}{\pi}e_{26}^{\theta}\bar{s}_{12}^{(1)}.
\end{aligned}
\tag{26}
$$

And the constitutive equations in the non-electrode region are derived:

$$
\begin{aligned}
T_{12}^{(0)} &= 4c_{66}^{\theta}s_{12}^{(0)} + 4c_{56}^{\theta}s_{13}^{(0)} + \frac{8}{\pi}c_{66}^{\theta}\bar{s}_{12}^{(1)} - \frac{4}{\pi}e_{26}^{\theta}\bar{E}_{2}^{(1)},\\
T_{13}^{(0)} &= 4c_{56}^{\theta}s_{12}^{(0)} + 4c_{55}^{\theta}s_{13}^{(0)} + \frac{8}{\pi}c_{56}^{\theta}\bar{s}_{12}^{(1)} - \frac{4}{\pi}e_{25}^{\theta}\bar{E}_{2}^{(1)},\\
T_{11}^{(1)} &= \bar{c}_{11}^{\theta}s_{11}^{(1)} - \bar{e}_{11}^{\theta}E_{1}^{(1)},\\
\bar{T}_{21}^{(1)} &= 2c_{66}^{\theta}\bar{s}_{12}^{(1)} - e_{26}^{\theta}\bar{E}_{2}^{(1)} + \frac{8}{\pi}c_{66}^{\theta}s_{12}^{(0)} + \frac{8}{\pi}c_{56}^{\theta}s_{13}^{(0)},\\
D_{1}^{(1)} &= \bar{e}_{11}^{\theta}s_{11}^{(1)} + \bar{\varepsilon}_{11}^{\theta}E_{1}^{(1)},\\
\bar{D}_{2}^{(1)} &= 2e_{26}^{\theta}\bar{s}_{12}^{(1)} + \varepsilon_{22}^{\theta}\bar{E}_{2}^{(1)} + \frac{8}{\pi}e_{26}^{\theta}s_{12}^{(0)} + \frac{8}{\pi}e_{25}^{\theta}s_{13}^{(0)}.
\end{aligned}
\tag{27}
$$

Using the stress-relief method [26], the equivalent elastic, piezoelectric, and dielectric coefficients of quartz for the plate equations are mathematically formulated as follows:

$$
\begin{aligned}
\bar{c}_{ijkl}^{\theta} &= [c_{ijkl}^{\theta} - \frac{(c_{ij22}^{\theta}\beta_{22} + c_{ij23}^{\theta}\beta_{23})c_{ij22}^{\theta}}{(c_{2222}^{\theta}\beta_{22} + c_{2223}^{\theta}\beta_{23})}],\\
\bar{e}_{kij}^{\theta} &= [e_{kij}^{\theta} - \frac{(c_{ij22}^{\theta}\beta_{22} + c_{ij23}^{\theta}\beta_{23})e_{k22}^{\theta}}{(c_{2222}^{\theta}\beta_{22} + c_{2223}^{\theta}\beta_{23})}],\\
\bar{\varepsilon}_{ik}^{\theta} &= [\varepsilon_{ik}^{\theta} + \frac{(e_{i22}^{\theta}\beta_{22} + e_{i23}^{\theta}\beta_{23})e_{k22}^{\theta}}{(c_{2222}^{\theta}\beta_{22} + c_{2223}^{\theta}\beta_{23})}).
\end{aligned}
\tag{28}
$$

Correspondingly, the modified constitutive equations are given by Eq. (29):

$$
\begin{cases}
T_{11}^{(1)} = \bar{c}_{11}^{\theta}s_{11}^{(1)} - \dfrac{8}{3\pi}\bar{e}_{11}^{\theta}E_{1}^{(2)},\\
\bar{D}_{1}^{(2)} = \dfrac{8}{3\pi}\bar{e}_{11}^{\theta}s_{11}^{(1)} + \bar{\varepsilon}_{11}^{\theta}E_{1}^{(2)},
\end{cases}
\quad \text{(with electrode)}
\tag{29}
$$

$$
\begin{cases}
T_{11}^{(1)} = \bar{c}_{11}^{\theta}s_{11}^{(1)} - \bar{e}_{11}^{\theta}E_{1}^{(1)},\\
D_{1}^{(1)} = \bar{e}_{11}^{\theta}s_{11}^{(1)} + \bar{\varepsilon}_{11}^{\theta}E_{1}^{(1)}.
\end{cases}
\quad \text{(without electrode)}
$$

For low-frequency bending vibrations of the plate or vibrations induced by the quasi-static bending with traction-free faces, the adjustment of shear stress is reported in [24]:

$$
T_{2a}^{(0)} = \frac{\pi^{3}}{24}\bar{T}_{2a}^{(1)}.
\tag{30}
$$

4. Dispersion Relations

Both the resonant frequencies and the vibration modes of the quartz plate can be determined by the dispersion curves. By comparing the dispersion curves predicted by the Lee plate theory with those obtained from 3D elastic theory, the validity and accuracy of the simplified plate model can be critically assessed. Furthermore, the coupled governing differential equations are formulated through the simultaneous solution of Eqs. (18)-(30), thereby providing the theoretical foundation for subsequent vibration and frequency analyses.

From the governing differential equations, the displacement field and electric potential with electrode can be expressed in the following assumed forms:

$$u_2^{(0)}=A_1\sin(\xi x_1)e^{i\omega t},\ u_3^{(0)}=A_2\sin(\xi x_1)e^{i\omega t},\ u_1^{(1)}=A_3\cos(\xi x_1)e^{i\omega t},\ \phi^{(2)}=\sqrt{\frac{c_{66}}{\varepsilon_{22}}}A_4\cos(\xi x_1)e^{i\omega t}. \quad (31)$$

The displacement and electric potential without electrode are assumed as follows:

$$u_2^{(0)}=A_1\cos(\xi x_1)e^{i\omega t},\ u_3^{(0)}=A_2\cos(\xi x_1)e^{i\omega t},\ u_1^{(1)}=A_3\sin(\xi x_1)e^{i\omega t},\ \phi^{(1)}=\sqrt{\frac{c_{66}}{\varepsilon_{22}}}A_4\sin(\xi x_1)e^{i\omega t}. \quad (32)$$

where, A_1, A_2, A_3, and A_4 are undetermined constants, k is the wave number in the x_1 direction, i is the imaginary unit, and ω is the frequency. The frequency, wave number, and material parameters are nondimensionalized [39] as follows:

$$\begin{aligned} &\omega^2=\Omega^2\frac{\pi^2}{4b^2}\frac{\bar{c}_{66}^{\theta}}{\rho},\quad \xi=Z\frac{\pi}{2b},\\ &\text{℘}_{pq}^{\theta}=\frac{\bar{c}_{pq}^{\theta}}{\bar{c}_{66}^{\theta}},\quad \text{℘}_{pq}^{\theta}=\frac{\bar{e}_{pq}^{\theta}}{(\bar{c}_{66}^{\theta}\bar{\varepsilon}_{22}^{\theta})^{1/2}},\quad \text{℘}_{pq}^{\theta}=\frac{\bar{\varepsilon}_{pq}^{\theta}}{\bar{\varepsilon}_{22}^{\theta}}. \end{aligned} \quad (33)$$

where Ω and Z are the dimensionless frequency and wave number, respectively.

By substituting the assumed displacements and potentials into the governing

differential equations, a homogeneous linear system in terms of the independent variables is obtained. Nontrivial solutions exist only when the determinant of the coefficient matrix vanishes, thereby yielding the dispersion relation.

$$\det([\Omega,\ Z]_{4\times4}) = 0 \tag{34}$$

As shown in Fig. 3, the dispersion curves for mass ratios of 0 and 0.01, corresponding to the unelectroded and electroded models, are presented. For comparison, the dispersion curves are also calculated based on the piezoelectric elastic theory, as indicated by the black lines in Fig. 3. The results indicate that the dispersion curves derived from the Lee plate equations are in excellent agreement with those obtained from the elastic equations, without any correction factors. In particular, both sets of dispersion curves agree closely near the cutoff frequency of the thickness-shear mode, i.e., in the long-wavelength range.

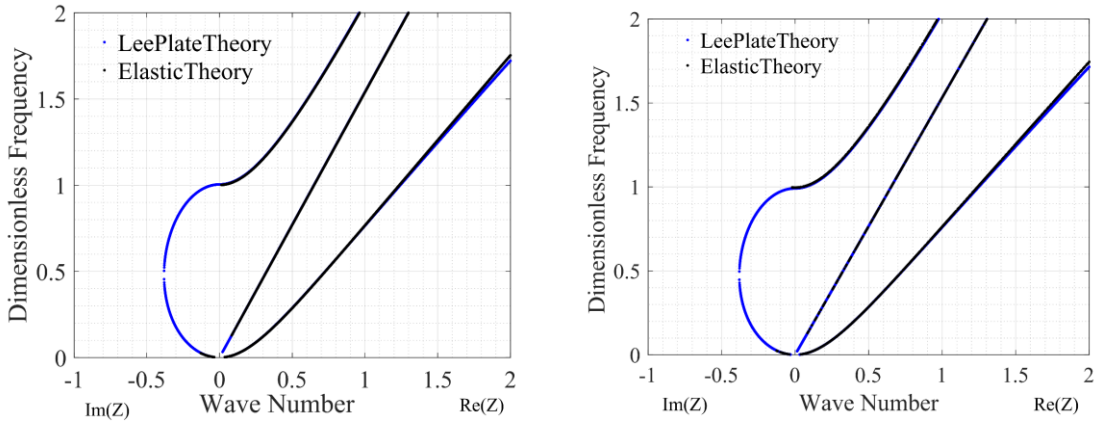

(a) (b)

Fig. 3. Dispersion curves: (a) without electrode: $R = 0$, (b) with electrode: $R = 0.01$.

5. Free vibrations

In the investigation of QCM with external temperature variations, mass sensitivity represents the most critical performance indicator. The concept originates from Günter Sauerbrey, who established a quantitative relationship between the frequency shift and the adsorbed mass change, known as the Sauerbrey equation [7].

$$\begin{aligned} \Delta f &= -\frac{2f_0^2 \Delta m}{A\sqrt{\rho_q \mu_q}} = -C_f \Delta m, \\ C_f &= \frac{2f_0^2}{A\sqrt{\rho_q \mu_q}}. \end{aligned} \tag{35}$$

where, f_0 is the resonant frequency of the QCM, μ_q represents the shear modulus of quartz, and C_f denotes the mass sensitivity coefficient. These parameters are all temperature dependent. A is the electrode area, and Δm is the adsorbed mass on the electrode surface. Considering only the mass effect, Δm is equivalently represented by the mass ratio R_g between the adsorbed layer and the quartz crystal plate. Δf indicates the resonant frequency shift induced by the adsorbed mass. The negative sign in Eq. (35) reflects that an increase in adsorbed mass results in a reduction of the QCM resonant frequency.

The frequency spectra for various adsorbed mass ratios are shown in Fig. 4. As the adsorbed mass ratio increases, the resonant frequency slightly decreases because the additional surface mass increases the effective inertia of the vibrating plate. In contrast, the spurious modes exhibit only minor frequency variations, indicating that the primary thickness-shear mode is more sensitive to surface mass loading than the other modes. To further investigate the influence of temperature on QCM sensitivity, sensitivity-

temperature relationships for different plate length-to-thickness ratios are analyzed under strong and weak mode coupling, respectively, as presented in Fig. 5.

Using the sensitivity-temperature curve for the weak mode coupling (l_q/h_q = 134), shown as the black line, the sensitivity varies smoothly with temperature and exhibits a single-valued relationship. This indicates that the operating mode remains well isolated from adjacent spurious modes, and the device maintains stable sensing performance over the entire temperature range. In contrast, for the strong mode coupling between the TSh and F modes (l_q/h_q = 133.48), shown as the red line, two closely spaced sensitivity values appear within a certain temperature range, indicating a loss of QCM sensitivity. This phenomenon arises from the mode interaction, where the vibration energy is redistributed between the coupled modes. As a result, the effective mass sensitivity of the QCM becomes ambiguous within this temperature interval. A similar phenomenon is observed for the TSh-FS mode coupling (l_q/h_q = 135.96), shown as the blue line, although the affected temperature interval is relatively narrower. The comparison indicates that the TSh-F mode interaction induces a broader sensitivity-loss region than the TSh-FS coupling, confirming that mode coupling is the main physical mechanism for the loss of sensitivity in the device

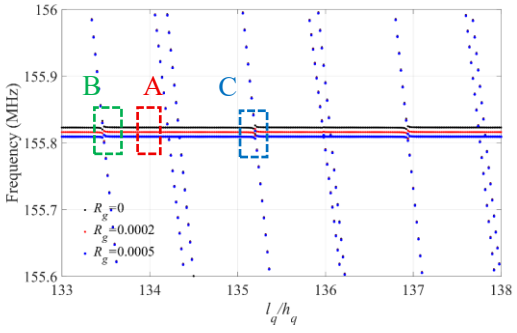

(a)

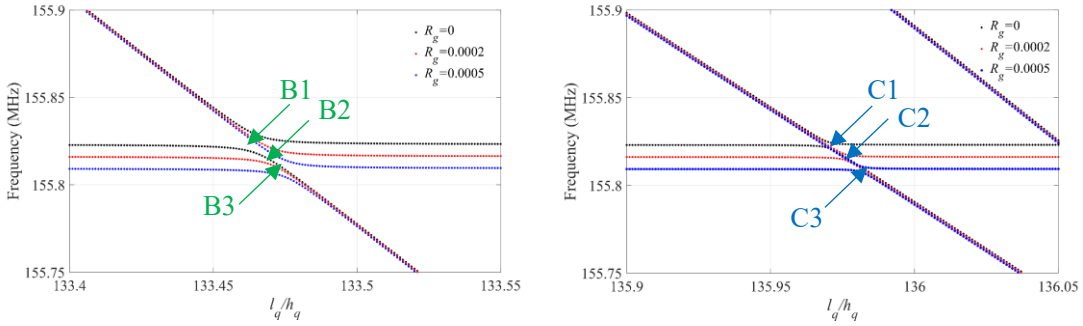

(b) (c)

Fig. 4. Spectra of QCM for different adsorbed mass ratios: (a) Large range. (b) The green and blue box in (a) are enlarged in (b) and (c), respectively. Different sample points in regions A and B are selected.

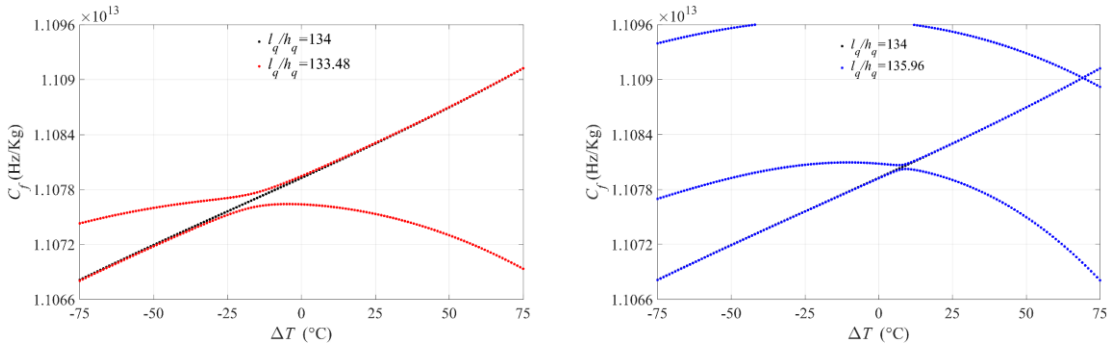

(a) (b)

Fig. 5. Sensitivity-temperature curves for different aspect ratios with $R_g = 0$: (a) l_q/h_q = 134 and l_q/h_q = 133.48, (b) l_q/h_q = 134 and l_q/h_q = 135.96.

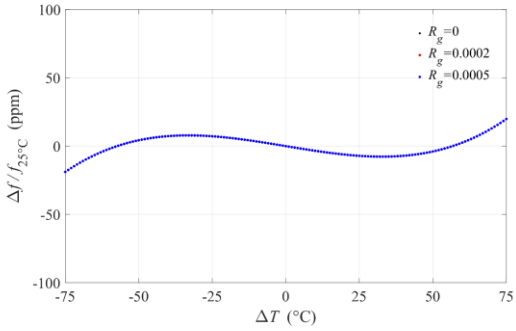

(a)

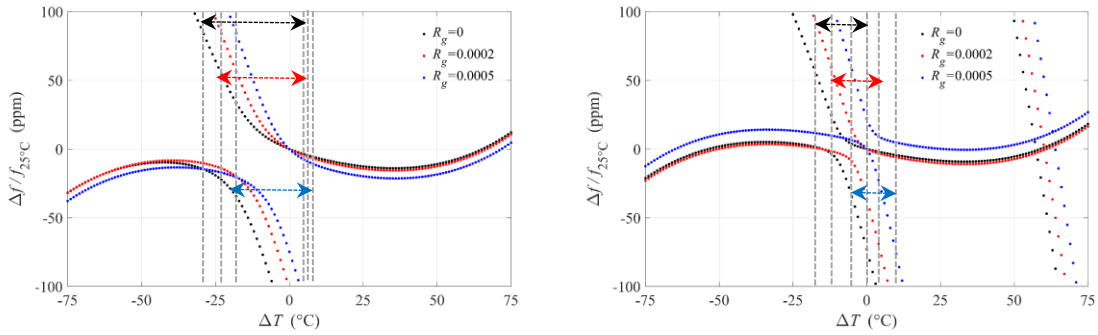

(b) (c)

Fig. 6. Frequency-temperature curves for different adsorbed mass ratios: (a) l_q/h_q = 134, (b) l_q/h_q = 133.48, (c) l_q/h_q = 135.96.

To further understand how mode coupling affects the frequency-temperature behavior, Fig. 6 presents the frequency-temperature curves for different aspect ratios corresponding to weak mode coupling (region A) and strong mode coupling (regions B and C). As shown in Fig. 7(a), when the device operates in the weak coupling region, the frequency varies smoothly with temperature and the effect of the adsorbed mass ratio mainly appears as a small vertical shift in the frequency-temperature curves. However, when the aspect ratio enters the strong coupling regions, the frequency-temperature curves exhibit abrupt variations. As shown in Fig. 7(b), the TSh-F mode coupling corresponding to B1, B2, and B3 in Fig. 4(b) produces a pronounced distortion in the frequency-temperature curves. In this region, the rapid frequency variation with temperature results in the well-known activity dip phenomenon. This behavior originates from the exchange of modal dominance between the interacting modes as temperature changes, which significantly alters the resonant response of the device.

Similarly, Fig. 7(c) shows the frequency-temperature curves associated with TSh-FS mode coupling for the aspect ratios C1, C2, and C3 indicated in Fig. 4(c). Although a comparable activity dip phenomenon is observed, the temperature interval in which this instability occurs is noticeably narrower than that in the TSh-F coupling case. Furthermore, increasing the adsorbed mass primarily shifts the frequency curves but has little influence on the temperature range where the activity dip occurs. This indicates that the instability is mainly governed by the intrinsic mode coupling characteristics determined by the plate geometry rather than by the surface mass loading. Overall, the results demonstrate that strong mode coupling significantly modifies both the sensitivity-temperature and frequency-temperature characteristics of high-frequency QCMs. In particular, the TSh-F mode interaction produces more pronounced instability and broader temperature regions of sensitivity loss and activity dips compared with the TSh-FS coupling case. These findings are consistent with the sensitivity analysis, confirming that strong mode coupling leads to more severe device instability.

6. Forced vibrations

To analyze the electrical responses of quartz crystal plate under thickness-mode excitation, an alternating voltage is applied across the electrodes. In the derivation of the two-dimensional Lee plate equations, these driving terms are incorporated through the first two terms in the potential. In addition, temperature-induced variations in the

resonant frequency of the quartz plate affect the electrical response, such as admittance and phase.

The forced vibrations are considered with an alternating voltage [39]:

$$\phi(t)|_{x_2=\pm b} = \mathrm{m}\phi_0 e^{i\omega t} \tag{36}$$

Substituting Eq. (36) into Eq. (23) yields:

$$B(t) = -\phi_0 e^{i\omega t} \tag{37}$$

where ϕ_0 is the applied voltage and ϕ_0 = 3V.

The total charge on the top electrode and the corresponding current [40] are

$$I = \dot{Q} = i\omega Q \tag{38}$$

In the first-order Lee plate theory, the electric displacement D_2 is approximated by its first-order component, and the relationship is

$$\bar{D}_2^{(1)} = \int_{-1}^{1} D_2 \sin\frac{\pi}{2}(1-\psi)d\psi = \frac{4}{\pi}D_2 \tag{39}$$

Finally, the admittance per unit area in the electrode within the Lee plate theory can be calculated by:

$$Y = \frac{\pi}{4}\frac{i\omega}{l_e}\frac{\int_{-l_e/2}^{l_e/2}\bar{D}_2^{(1)}dx_1}{\phi_0} \tag{40}$$

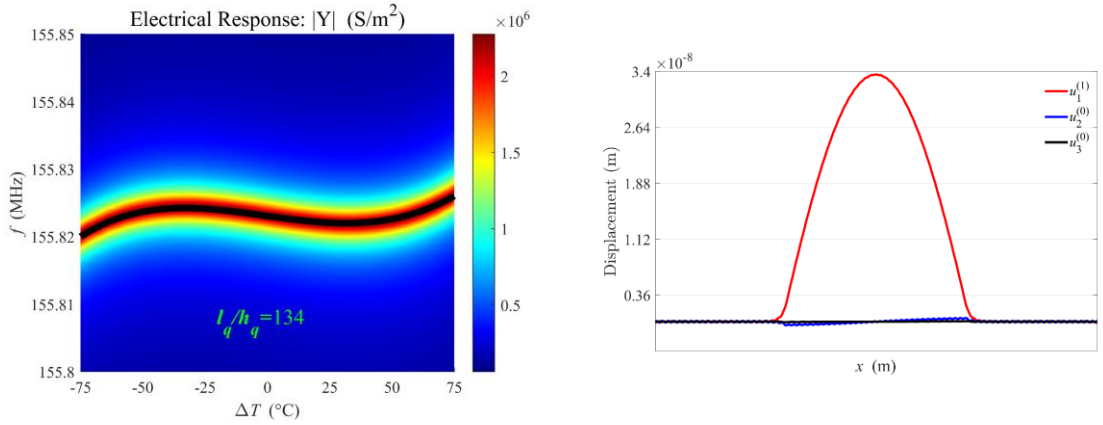

(a)

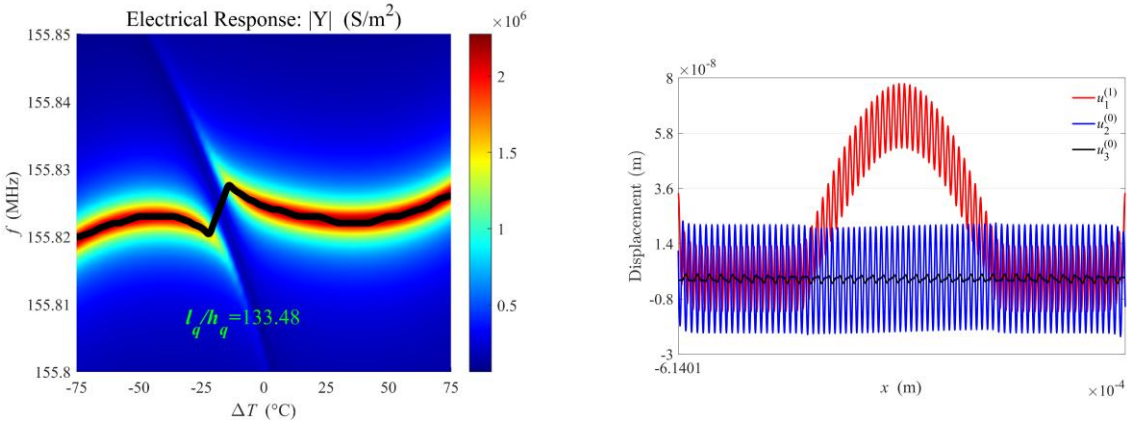

(b)

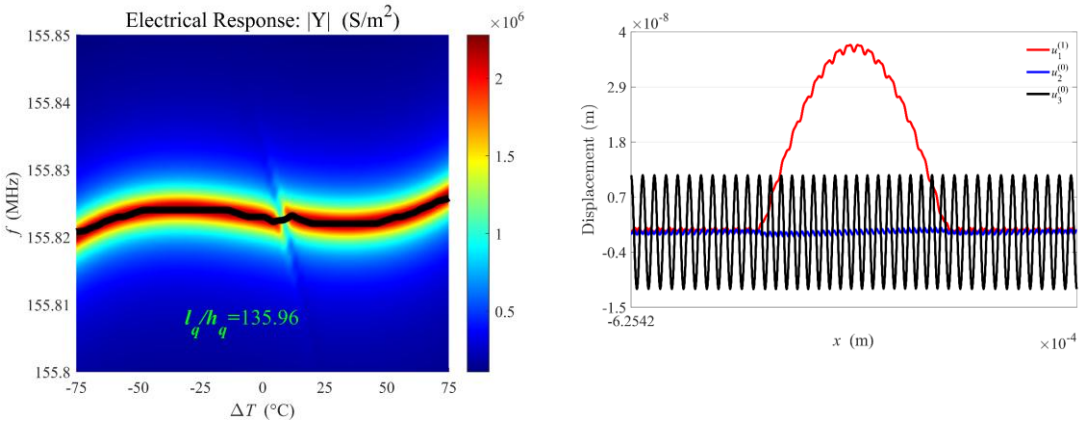

(c)

Fig. 7. Admittance response and corresponding displacement for different aspect ratios with $R_g = 0$: (a) $l_q/h_q = 134$, (b) $l_q/h_q = 133.48$, (c) $l_q/h_q = 135.98$.

Fig. 7 illustrates the variation of the admittance response with temperature change ΔT and resonant frequency f, along with the corresponding displacement distributions. Fig. 7(a) shows the result of weak mode coupling, while Figs. 7(b) and 7(c) correspond to strong mode coupling for TSh-F and TSh-FS mode, respectively. As seen in Fig. 7(a), the admittance amplitude shows a smooth cubic-like curve as the temperature changes, while the displacement distribution reveals that the vibration is mainly confined in the

electroded region, consistent with the energy-trapping effect. However, in Figs. 7(b) and 7(c), the admittance amplitude exhibits anomalies over temperature ranges, and the displacement of the ripples is no longer consistent with the energy trapping. It indicates that the electrical stability is not reliable with strong mode coupling. The results also agree well with the frequency-temperature characteristic analysis.

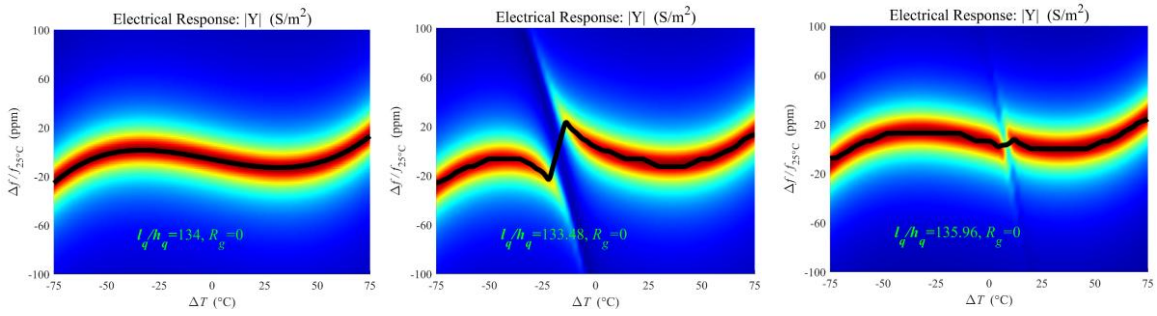

(a)

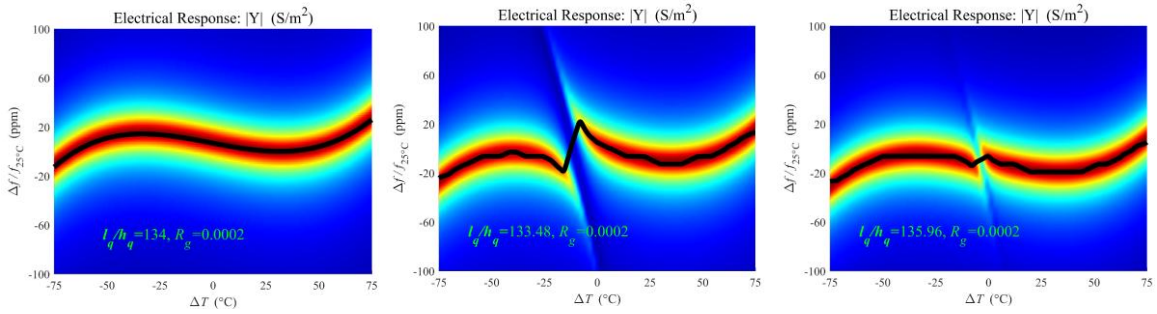

(b)

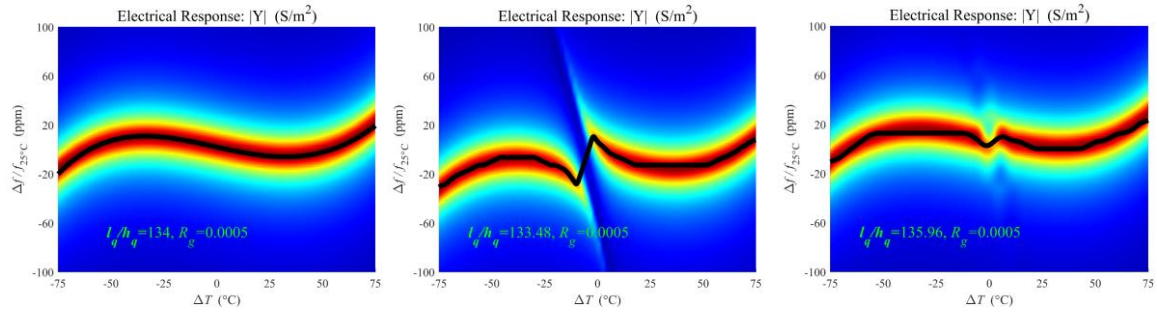

(c)

Fig. 8. Admittance response for different aspect ratios and adsorbed mass ratios: (a) $R_g = 0$, (b) $R_g = 0.0002$, (c) $R_g = 0.0005$.

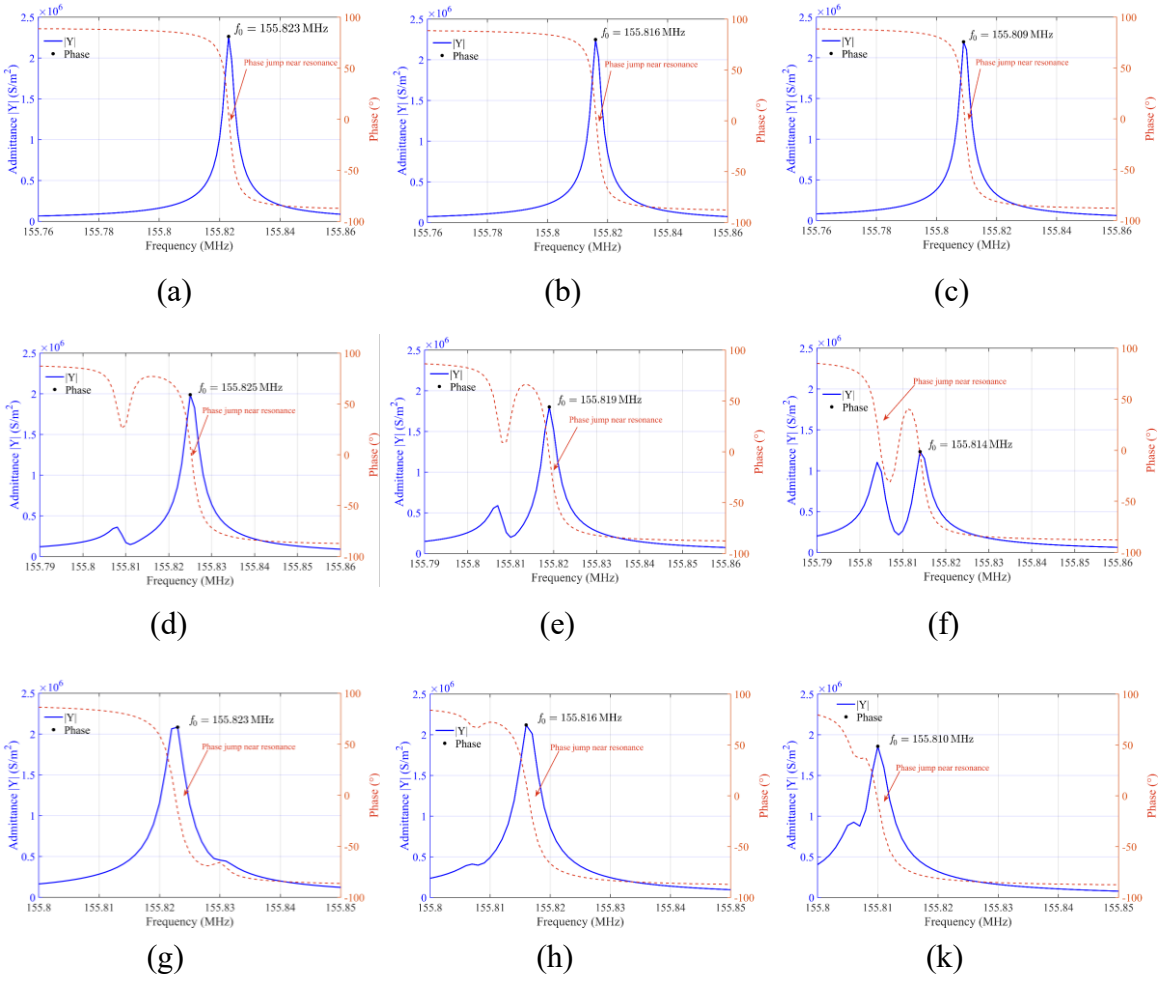

Fig. 9. Electrical response: admittance (blue line) and phase (red dot line). l_q/h_q =134, ΔT = 0°: (a) R_g = 0, (b) R_g = 0.0002, (c) R_g = 0.0005. l_q/h_q = 133.48, ΔT = -5°: (d) R_g = 0, (e) R_g = 0.0002, (f) R_g = 0.0005. l_q/h_q = 135.96, ΔT = 3°: (g) R_g = 0, (h) R_g = 0.0002, (k) R_g = 0.0005.

A set of admittance response curves for various absorbed masses is shown in Fig. 8 to analyze how mode coupling affects the electrical stability of the QCM. The black curve represents the variation of the resonant frequency corresponding to the admittance peak as a function of temperature. For high-frequency QCM, the variation range of the adsorbed mass is relatively small. Therefore, under comparable aspect ratios, the overall patterns of the abnormal admittance responses remain nearly

unchanged. As the absorbed mass increases, the resonant frequency shifts slightly due to the increase in effective inertia, while the mode coupling behavior remains essentially the same. Comparing Fig. 8 with Fig. 6, the trends of the curves and the temperature ranges corresponding to the activity dip remain nearly identical. This indicates that the temperature-induced mode coupling dominates the electrical response of the device, while the influence of the absorbed mass mainly results in a small frequency shift. These results confirm that strong mode coupling can induce temperature-dependent activity dip and anomalous admittance amplitude, which may reduce the electrical stability of the QCM.

As shown in Figs. 9(a)-(c), with weak mode decoupling, the admittance and phase change smoothly with the temperature. However, in Figs. 9(d)-(k) with strong mode coupling, the value of admittance and phase increase or decrease significantly with temperature. The electrical stability with strong mode coupling is more strongly affected by the mass of absorbed layer. There are some ripples around the resonant frequency, which is induced by spurious modes. For QCM, the ripples of the admittance and phase will affect the stability of the electric response, to result in the output of the electrical parameters. It is evidence that the mode coupling between the TSh and F modes causes the most severe instability. Since the quality factor Q is proportional to the phase slope $\partial\varphi/\partial f$ [41], perturbations in the phase response can directly modify the resonator's energy dissipation characteristics. It means the perturbations induced by strong mode coupling affect the Q value. A decrease in Q results in a broader admittance peak, reduced frequency stability, and increased energy loss, leading to degraded mass

sensitivity and higher noise in QCM measurements. Therefore, in QCM design under temperature variations, aspect ratios that are prone to causing mode coupling with the F mode should be avoided.

7. Conclusions

This study employs the first-order Lee plate theory considering a temperature bias field to analyze the vibrational and electrical characteristics of high-frequency quartz crystal microbalances (QCMs). Dispersion analysis of an infinite quartz plate confirms the accuracy of the developed model, demonstrating excellent agreement with the three-dimensional piezoelectric elastic theory. As no correction factors are required for these formulations, the developed model provides a reliable approach for describing thickness-shear vibrations under thermal effects.

Results show that temperature variations significantly influence mode interactions in finite QCMs. Strong coupling between thickness-shear and flexural modes, as well as between thickness-shear and face-shear modes, causes the pronounced loss of mass sensitivity within specific temperature ranges. These coupling effects lead to rapid frequency shifts and activity dips, indicating that mode coupling plays a more dominant role in the loss of mass sensitivity, as compared with the effect on the absorbed mass.

In addition to shifting the resonant frequency, the adsorbed mass also influences electrical stability with strong mode coupling. Anomalous admittance responses and phase perturbations appear near the coupling regions, resulting in the reduced frequency

stability and degraded sensing performance. These findings provide quantitative guidance to select appropriate aspect ratios and operating temperature ranges for the improved temperature stability in high-frequency QCMs.

CRediT authorship contribution statement

Mengjie Li: Writing -- original draft, Methodology, Investigation, Formal analysis, Conceptualization. **Nian Li**: Writing -- review & editing, Validation, Supervision, Conceptualization. **Peng Li**: Investigation, Conceptualization. **Hirotsugu Inoue**: Writing -- review & editing, Supervision. **Iren Kuznetsova**: Funding acquisition, Conceptualization. **Dianzi Liu**: Writing -- review & editing, Supervision. **Zhenghua Qian**: Writing - review & editing, Supervision, Funding acquisition, Conceptualization.

Declaration of competing interest

The authors declare that they have no known competing financial interests or personal relationships that could have appeared to influence the work reported in this paper.

Acknowledgments

This work was supported by the National Key Research and Development

Program of China (grant number 2023YFE0111000), the National Natural Science Foundation of China (grant numbers 12372151, 12172171, and U24A2005), Shenzhen Science and Technology Program (grant number JCYJ20230807142004009), Shenzhen Longhua Science and Technology Innovation Special Funding Project (Industrial Sci-Tech Innovation Center of Low-Altitude Intelligent Networking) and was partially supported by Russian Ministry of Science and Higher Education. The first author is grateful for the financial support from the China Scholarship Council (CSC).

Data availability

Data will be made available on request.

Reference

[1] A. D. Easley, T. Ma, C. I. Eneh, et al., A practical guide to quartz crystal microbalance with dissipation monitoring of thin polymer films, J. Polym. Sci. 60 (2021) 1090-1107. https://doi.org/10.1002/pol.20210324.

[2] Y. P. Kong, J. X. Liu, H. J. He, J. S. Yang, Effects of mass layer dimension on a finite quartz crystal Microbalance, Acta Mech. 222 (2011) 103-113. https://doi.org/10.1007/s00707-011-0522-y.

[3] J. Yao, B. Feng, Z. Q. Zhang, et al., Blood coagulation testing smartphone platform using quartz crystal microbalance dissipation method, Sensors. 18 (2018) 3073. https://doi.org/10.3390/s18093073.

[4] K. M. Hoffmann, A. Langhoff, J. Adams, et al., Differences in emulsion polymerization fouling between acrylates and vinyl acetate studied in-situ with a quartz crystal microbalance (QCM), Heat Mass Trans. 61 (2025) 79. https://doi.org/10.1007/s00231-025-03597-x.

[5] Y. Yao, X. H. Huang, B. Y. Zhang, Z. Zhang, D. Hou, Z. K. Zhou, Facile fabrication of high sensitivity cellulose nanocrystals based QCM humidity sensors with asymmetric electrode structure, Sens. Actuators B, Chem. 302 (2020) 127192. https://doi.org/10.1016/j.snb.2019.127192.

[6] S. N. Songkhla, T. Nakamoto, Overview of quartz crystal microbalance behavior analysis and measurement, Chemosensors. 9 (2021) 350. https://doi.org/10.3390/chemosensors9120350.

[7] G. Sauerbrey, Verwendung von schwingquarzen zur wägung dünner schichten und zur mikrowägung, Z. Phy. A. 155 (1959) 206-222. https://doi.org/10.1007/BF01337937.

[8] G. G. Guilbault, A. Lopez-Roman, Use of sodium tetrachloromercuriate as a substrate for the determination of So2 on the piezocrystal detector, Environ. Lett. 2 (1971) 35-45. https://doi.org/10.1080/00139307109435424.

[9] J. Hlavay, G. G. Guilbault, Applications of the piezoelectric crystal detector in analytical chemistry, Anal. Chem. 49 (1977) 1890-1898. https://doi.org/10.1021/ac50021a007.

[10] C. March, J. V. Garcí, Á. Sánchez, et al., High-frequency phase shift measurement greatly enhances the sensitivity of QCM immunosensors, Biosens. Bioelectron. 65 (2015) 1-8. https://doi.org/10.1016/j.bios.2014.10.001.

[11] P. C. Y. Lee, Y. K. Yong, Frequency-temperature behavior of thickness vibrations of doubly rotated quartz plates affected by plate dimensions and orientations, J. Appl. Phys. 60 (1986) 2327-2342. https://doi.org/10.1063/1.337143.

[12] M. J. Li, P. Li, N. Li, D. Z. Liu, I. E. Kuznetsova, Z. H. Qian, Surface roughness effects on the vibration characteristics of AT-cut quartz crystal plate, Sensors. 23 (2023) 5168. https://doi.org/10.3390/s23115168.

[13] M. J. Li, N. Li, P. Li, et al., The multi-field coupled vibration analysis of AT-cut quartz crystal resonators with parallelism error, Acta Mech. Solida Sin. 36 (2023) 349-360. https://doi.org/10.1007/s10338-023-00384-1.

[14] Q. Huang, J. Wang, N. Gan, et al., An analysis of the thermal behavior and effects of circular quartz crystal resonators for microbalance applications, IEEE Trans. Ultrason. Ferroelectr. Freq. Contr. 69 (2022) 2569-2578. https://doi.org/10.1109/TUFFC.2022.3182878.

[15] Y. K. Yong, J. Vig, A. Ballato, R. Kubena, R. M. Closkey, Frequency-temperature analysis of MEMS AT-cut quartz resonators, in: 2003 IEEE International Frequency Control Symposium and PDA Exhibition Jointly with the 17th European Frequency and Time Forum, 2003, pp. 1095-1099. https://doi.org/10.1109/FREQ.2003.1275244.

[16] H. Satani, K. Yasuda, M. Sohgawa, T. Abe, Temperature characteristics of a thickness shear mode quartz crystal resonator bonded to a support substrate, Appl. Phys. Lett. 121 (2022) 252903. https://doi.org/10.1063/5.0132804.

[17] R. X. Wu, W. J. Wang, G. J. Chen, J. K. Du, T. F. Ma, J. Wang, Frequency-temperature analysis of thickness-shear vibrations of SC-cut quartz crystal plates with

the First-order Mindlin plate equations, Acta Mech. Solida Sin. 34 (2021) 516-526. https://doi.org/10.1007/s10338-021-00224-0.

[18] J. K. Du, W. J. Wang, G. J. Chen, et al., An analysis of Thickness-shear vibrations of doubly-rotated quartz crystal plates with the corrected First-order Mindlin plate equations, IEEE Trans. Ultrason. Ferroelectr. Freq. Contr. 60 (2013) 2371-2380. http://dx.doi.org/10.1109/TUFFc.2013.2833.

[19] I. A. Abbas, Three-phase lag model on thermoelastic interaction in an unbounded fiber-reinforced anisotropic medium with a cylindrical cavity, J. Comput. Theor. Nanosci. 11 (2014) 987-992. http://dx.doi.org/10.1166/jctn.2014.3454.

[20] M. I. Marin, R. P. Agarwal, I. A. Abbas, Effect of intrinsic rotations, microstructural expansion and contractions in initial boundary value problem of thermoelastic bodies, Bound. Value Probl. 2014 (2014) 1-16. http://dx.doi.org/10.1186/1687-2770-2014-129.

[21] I. A. Abbas, R. Kumar, Response of thermal source in initially stressed generalized thermoelastic half-space with voids, J. Comput. Theor. Nanosci. 11 (2014) 1472-1479. http://dx.doi.org/10.1166/jctn.2014.3520.

[22] A. E. Abouelregal, M. Marin, A. Öchsner, The influence of a non-local Moore-Gibson-Thompson heat transfer model on an underlying thermoelastic material under the model of memory-dependent derivatives, Contin. Mech. Thermodyn. 35 (2023) 545-562. http://dx.doi.org/10.1007/s00161-023-01195-y.

[23] S. Sadighi, M. Marin, An in-depth theoretical investigation of biomagnetic fluid flow and heat-mass transfer on a porous stretching/shrinking cylinder hosting motile

gyrotactic microorganisms, Int. J. Numer. Methods Heat Fluid Flow. 36 (2025) 1-22. http://dx.doi.org/ 10.1108/HFF-09-2025-0671.

[24] P. C. Y. Lee, Z. Nikodem, An approximation theory for high-frequency vibrations of elastic plate, Int. J. Solids Structures. 8 (1972) 581-612. https://doi.org/10.1007/s10778-025-01354-5.

[25] Z. Nikodem, Approximate theory of vibration of crystal plates at high frequencies, Int. J. Solids Structures. 10 (1974) 177-196. https://doi.org/10.1016/0020-7683(74)90017-1.

[26] P. C. Y Lee, J. D Yu, W. S Lin, A new two-dimensional theory for vibrations of piezoelectric crystal plates with electroded faces, J. Appl. Phys. 83 (1998) 1213-1223. https://doi.org/10.1063/1.366818.

[27] P. C. Y. Lee, R. Huang, Mechanical effects of electrodes on the vibrations of quartz crystal plates, IEEE Trans. Ultrason. Ferroelectr. Freq. Contr. 49 (2002) 612-625. http://dx.doi.org/10.1109/TUFFC.2002.1002460.

[28] P. C. Y. Lee, W. S. Lin, Piezoelectrically forced vibrations of electroded, doubly rotated crystal plates, J. Appl. Phys. 83 (1998) 7822-7833. https://doi.org/10.1063/1.367957.

[29] P. C. Y. Lee, An accurate two-dimensional theory of vibrations of isotropic, elastic plates, Acta Mech. Solida Sin. 24 (2011) 125-134. https://doi.org/10.1016/S0894-9166(11)60014-1.

[30] J. K. Du, W. J. Wang, G. J. Chen, et al., An analysis of thickness-shear vibrations of doubly-rotated quartz crystal plates with the corrected first-order Mindlin plate

equations, IEEE Trans. Ultrason. Ferroelectr. Freq. Contr. 60 (2013) 2371-2380. http://dx.doi.org/10.1109/TUFFC.2013.6644740.

[31] J. Wang, G. J. Chen, J. K. Du, Lee plate equations for electroded quartz crystal plates with the consideration of electrode density and stiffness, IEEE Trans. Ultrason. Ferroelectr. Freq. Contr. 55 (2008) 503-507. http://dx.doi.org/10.1109/TUFFC.2008.669.

[32] R. X. Wu, W. J. Wang, G. J. Chen, J. K. Du, T. F Ma, Ji Wang, Forced vibrations of SC-cut quartz crystal rectangular plates with partial electrodes by the Lee plate equations, Ultrasonics. 65 (2015) 338-344. https://doi.org/10.1016/j.ultras.2015.09.008.

[33] P. C. Y. Lee, Y. K. Yong, Frequency-temperature behavior of thickness vibrations of doubly rotated quartz plates affected by plate dimensions and orientations, J. Appl. Phys. 60 (1986) 2327-2342. https://doi.org/10.1063/1.337143.

[34] J. Wang, The frequency-temperature analysis equations of piezoelectric plates with Lee plate theory, IEEE Trans. Ultrason. Ferroelectr. Freq. Contr. 46 (1999) 1042-1046. http://dx.doi.org/10.1109/58.775672.

[35] Y. K. Yong, W. Wei, Lagrangian temperature coefficients of the piezoelectric stress constants and dielectric permittivity of quartz, in: 2000 IEEE/EIA International Frequency Control Symposium and Exhibition (Cat. No.00CH37052), 2000, pp. 364-372. http://dx.doi.org/10.1109/FREQ.2000.887383.

[36] H. F. Tiersten, Linear Piezoelectric Plate Vibrations, Plenum Press, New York, 1969.

[37] P. C. Y. Lee, S. Syngellakis, J. P. Hou, A two-dimensional theory for high-

frequency vibrations of piezoelectric crystal plates with or without electrodes, J. Appl. Phys. 61 (1987) 1249-1262. https://doi.org/10.1063/1.338102.

[38] R. D. Mindlin, Anharmonic, thickness-twist overtones of thickness-shear and flexural vibrations of rectangular, AT-cut quartz plates, J. Acoust. Soc. Am. 42 (1967) 1268. https://doi.org/10.1121/1.1910716.

[39] T. F. Ma, J. Wang, J. K. Du, J. S. Yang, Resonances and energy trapping in AT-cut quartz resonators operating with fast shear modes driven by lateral electric fields produced by surface electrodes, Ultrasonics. 59 (2015) 14-20. https://doi.org/10.1016/j.ultras.2015.01.004.

[40] N. Li, Z. H. Qian, B. Wang, Forced coupling vibration analysis of FBAR based on two-dimensional equations associated with state-vector approach, AIP Adv. 8 (2018) 095306. https://doi.org/10.1063/1.5046533.

[41] J. M. L. Miller, A. Ansari, D. B. Heinz, et al., Effective quality factor tuning mechanisms in micromechanical resonators, Appl. Phys. Rev. 5 (2018) 041307. https://doi.org/10.1063/1.5027850.

Appendix A

The main symbols and parameters used in this study are summarized below.

Nomenclature

$i, j, k, l, a, A_1, A_2, A_3, A_4$ = constants;

A	Electrode area;
c_{ijkl}^{θ}	Temperature-dependent elastic constant;
c_{ijkl}	Elastic constant at room temperature;
C_f	Mass sensitivity coefficient;
D_i	Electric displacement;
E_i	Electric field;

e_{ijk}^{θ} Temperature-dependent piezoelectric constant;
e_{ijk} Piezoelectric constant at room temperature;
f_0 Resonant frequency;
Δf Frequency shift;
h_q Thickness of quartz crystal plate;
h_{e1} Thickness of upper electrode;
h_{e2} Thickness of lower electrode;
I Current;
k Wave number;
l_q Length of quartz crystal plate;
l_e Length of electrode;
Δm Adsorbed mass;
n_i Unit outward normal;
Q Charge;
R_g Mass ratio between adsorbed layer and plate;
R Mass ratio between electrode and plate;
S_{ij} Strain;
T_{ij} Stress;
ΔT Temperature change;
t_j Surface traction;
u_i Displacement;
$u_i^{(n)}$ n-order Displacement components;
Y Admittance;
Z Dimensionless wave number.

Greek letters

$\alpha_{ik}^{(n)}$ nth-order Thermal expansion coefficients;
β_{ij} Thermal expansion coefficient;
$\varepsilon_{ij}^{\theta}$ Temperature-dependent dielectric constant;
ε_{ik} Dielectric constant at room temperature;
δ_{ik} Kronecker delta;
μ_q Shear modulus of quartz;
ρ Density;
σ Surface charge density;
ϕ Electric potential;
$\phi^{(n)}$ n-order Potential components;
ϕ_0 Applied voltage;
ω Frequency;
Ω Dimensionless frequency.